Nanowire dye-sensitized solar cells

MATT LAW[1,2]*, LORI E. GREENE[1,2]*, JUSTIN C. JOHNSON[1], RICHARD SAYKALLY[1] AND PEIDONG YANG[1,2]†

[1]Department of Chemistry, University of California, Berkeley, California 94720, USA
[2]Materials Science Division, Lawrence Berkeley National Laboratory, Berkeley, California 94720, USA
*These authors contributed equally to this work.
†e-mail: p_yang@berkeley.edu

Excitonic solar cells[1]—including organic, hybrid organic–inorganic and dye-sensitized cells (DSCs)—are promising devices for inexpensive, large-scale solar energy conversion. The DSC is currently the most efficient[2] and stable[3] excitonic photocell. Central to this device is a thick nanoparticle film that provides a large surface area for the adsorption of light-harvesting molecules. However, nanoparticle DSCs rely on trap-limited diffusion for electron transport, a slow mechanism that can limit device efficiency, especially at longer wavelengths. Here we introduce a version of the dye-sensitized cell in which the traditional nanoparticle film is replaced by a dense array of oriented, crystalline ZnO nanowires. The nanowire anode is synthesized by mild aqueous chemistry and features a surface area up to one-fifth as large as a nanoparticle cell. The direct electrical pathways provided by the nanowires ensure the rapid collection of carriers generated throughout the device, and a full Sun efficiency of 1.5% is demonstrated, limited primarily by the surface area of the nanowire array.

The anodes of dye-sensitized solar cells are typically constructed using thick films (~10 μm) of TiO$_2$ or, less often, SnO$_2$ or ZnO nanoparticles[4–6] that are deposited as a paste and sintered to produce electrical continuity. The nanoparticle film provides a large internal surface area (characterized by a roughness factor, defined as the total film area per unit substrate area, of ~1,000) for the anchoring of sufficient chromophore (usually a ruthenium-based dye) to yield high light absorption in the 400–800 nm region, where much of the solar flux is incident. During operation, photons intercepted by the dye monolayer create excitons that are rapidly split at the nanoparticle surface, with electrons injected into the nanoparticle film and holes leaving the opposite side of the device by means of redox species (traditionally the I$^-$/I$_3^-$ couple) in a liquid or solid-state[7] electrolyte. The classic report[8] of a 10% efficient TiO$_2$ DSC initiated a decade of research into the electrical transport physics of nanoparticle anodes, which were shown to collect injected electrons with high efficiency despite their disordered, polycrystalline topology.

The nature of electron transport in oxide nanoparticle films is fairly well understood. Time-resolved photocurrent and photovoltage measurements[9,10] and modelling studies[11,12] indicate that electron transport in wet, illuminated nanoparticle networks proceeds by a trap-limited diffusion process, in which photogenerated electrons repeatedly interact with a distribution of traps as they undertake a random walk through the film. Drift transport, a vital mechanism in most photovoltaic cells, is prevented in DSCs by ions in the electrolyte that screen macroscopic electric fields and couple strongly with the moving electrons, effectively rendering them neutral carriers (that is, there is ambipolar diffusion)[13]. Under full sunlight, an average injected electron may experience a million trapping events before either percolating to the collecting electrode or recombining with an oxidizing species, predominantly I$_3^-$ in the electrolyte[14]. Transit times for electron escape from the film average in the milliseconds[15]. Yet despite the extremely slow nature of such trap-mediated transport (characterized by an electron diffusivity, $D_n \leq 10^{-4}$ cm^2 s^{-1}, several orders of magnitude smaller than in TiO$_2$ and ZnO single crystals[16,17]), electron collection remains favoured over recombination because of the even slower multi-electron kinetics of I$_3^-$ reduction on oxide surfaces. Electron diffusion lengths of 7–30 μm have been reported for cells operating at light intensities up to 0.1 Sun[9,10,18]. This is strong evidence that electron collection is highly efficient for the 10-μm-thick nanoparticle films normally used in devices.

Insight into the factors that limit DSC performance is gained by comparing theoretical cell efficiencies with those of current state-of-the-art cells. The power conversion efficiency η of a solar cell is given as $\eta = (FF \times |J_{sc}| \times V_{oc})/P_{in}$, where FF is the fill factor, $|J_{sc}|$ is the absolute value of the current density at short circuit, V_{oc} is the photovoltage at open circuit and P_{in} is the incident light power density. In principle, the maximum J_{sc} of a DSC is determined by how well the absorption window of its dye overlaps the solar spectrum. Record cells achieve current densities (and overall efficiencies) that are between 55 and 75% of their theoretical maxima at full sunlight, depending on the exact dye used[19]. Much of the shortfall is due to the poor absorption of low-energy photons by available dyes. Considerable efforts have been made to develop dyes and dye mixtures that absorb better at long wavelengths[20,21], so far with little success. Another option for improving the absorption of red and near-infrared light—thickening the nanoparticle film to increase its optical density—is unsuccessful because the film thickness comes to exceed the electron diffusion length through the nanoparticle network.

One promising solution to this impasse is to increase the electron diffusion length in the anode by replacing the nanoparticle film with an array of oriented single-crystalline nanowires. Electron transport in crystalline wires is expected to be several orders of magnitude faster than percolation through a random polycrystalline network.
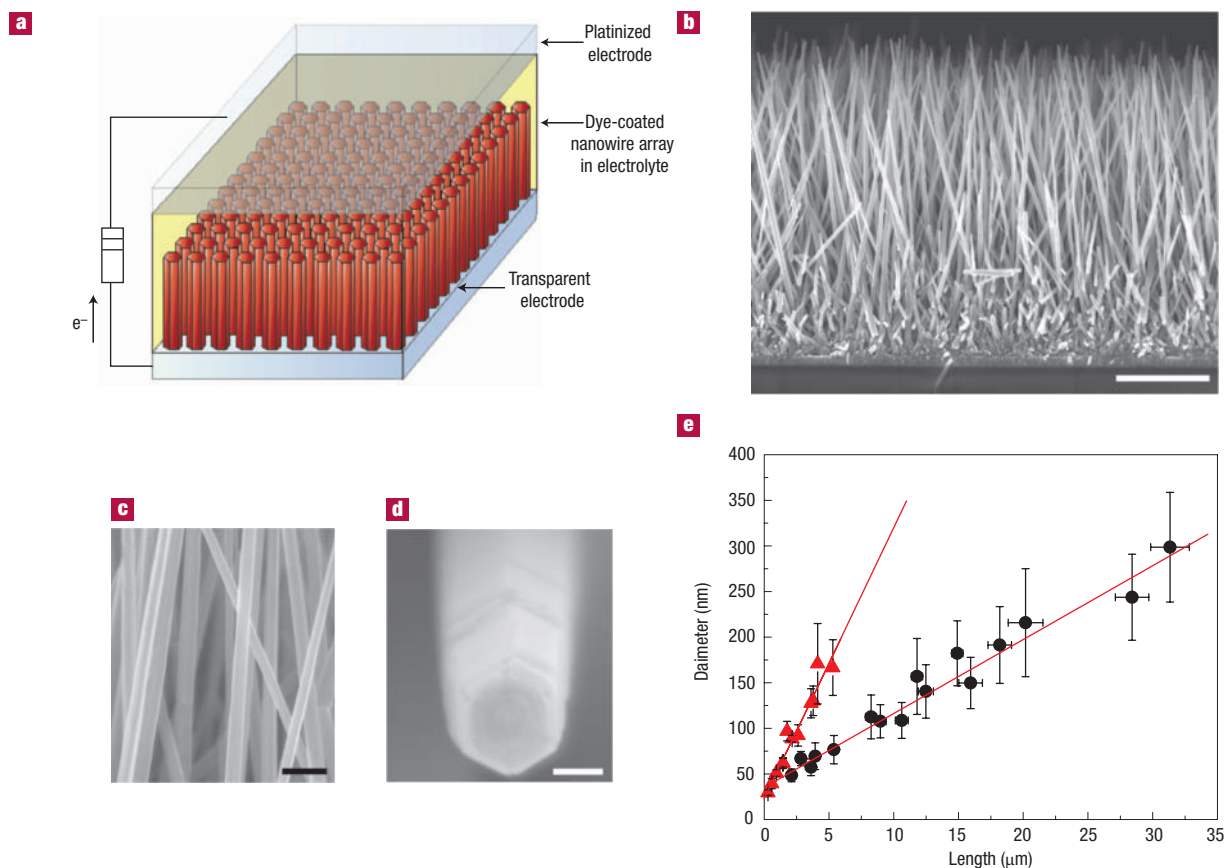
455

Figure 1 The nanowire dye-sensitized cell, based on a ZnO wire array. a, Schematic diagram of the cell. Light is incident through the bottom electrode. **b**, Typical scanning electron microscopy cross-section of a cleaved nanowire array on FTO. The wires are in direct contact with the substrate, with no intervening particle layer. Scale bar, 5 μm. **c**, Magnified view of the oriented wires. In this array, wire length and diameter vary from 16 to 17 μm and 130 to 200 nm, respectively. Scale bar, 500 nm. **d**, Typical top view of a single nanowire, showing its faceting, surface texture and a slight taper to its tip. Scale bar, 50 nm. **e**, Wire length against diameter with (circles) and without (triangles) PEI added to the growth bath. Lines are least-squares fits to the data, and error bars represent one standard deviation.

Using a sufficiently dense array of long, thin nanowires as a dye scaffold, it should be possible to increase the DSC dye loading (and so its absorption of red light) while simultaneously maintaining very efficient carrier collection. Moreover, the rapid transport provided by a nanowire anode would be particularly favourable for cell designs that use non-standard electrolytes, such as polymer gels or solid inorganic phases, in which recombination rates are high compared with the liquid electrolyte cell[22]. Here we present the first ordered nanowire DSC (Fig. 1a) and illustrate how this topology could improve the understanding and performance of DSCs and other types of excitonic solar cells.

A high-performance nanowire photoanode must foremost have a large surface area for dye adsorption, comparable to that of a nanoparticle film. We made ZnO nanowire arrays of high surface area in aqueous solution using a seeded growth process[23] that was modified to yield long wires. Briefly, a 10–15-nm-thick film of ZnO quantum dots was deposited onto F:SnO₂ conductive glass (FTO) substrates by dip coating, and wires were grown from these nuclei through the thermal decomposition of a zinc complex. This two-step process is a simple, low-temperature and environmentally benign route to forming dense arrays (up to 35 billion wires per square centimetre) on arbitrary substrates of any size. Solution-grown ZnO nanowire arrays reported previously have been limited to aspect ratios of less than 20, too small for efficient DSCs. We boosted the aspect ratio of our nanowires above 125 by using polyethylenimine (PEI), a cationic polyelectrolyte, to hinder only the lateral growth of the nanowires in solution, while maintaining a relatively high nanowire density (Fig. 1b–d and Methods). The striking effect of this molecule is seen by plotting nanowire length against diameter at different growth times with and without PEI (Fig. 1e). The longest arrays presented here (20–25 μm) have one-fifth the active surface area of a nanoparticle anode.

The wire films are good electrical conductors along the direction of the wire axes. Two-point electrical measurements of dry arrays on FTO substrates gave linear current–voltage (I–V) traces (see Supplementary Information, Fig. S1), indicating barrier-free contacts between nanowire and substrate. Individual nanowires were extracted from the arrays, fashioned into field-effect transistors using standard electron-beam lithography procedures, and analysed to determine their resistivity, carrier concentration and mobility (Fig. S2). Measured resistivity values ranged from 0.3 to 2.0 Ω cm, with an electron concentration of $1-5 \times 10^{18}$ cm⁻³ and mobility of $1-5$ cm² V⁻¹ s⁻¹. Using the Einstein relation, $D = k_B T \mu / e$, we estimate an electron diffusivity $D_n = 0.05$–0.5 cm² s⁻¹ for single dry nanowires. This value is several hundred times larger than the highest reported diffusivity for TiO₂ or ZnO nanoparticle films in operating cells[15,24]. Moreover, the conductivity of the wire arrays increased by 5–20% when they were bathed in the standard DSC
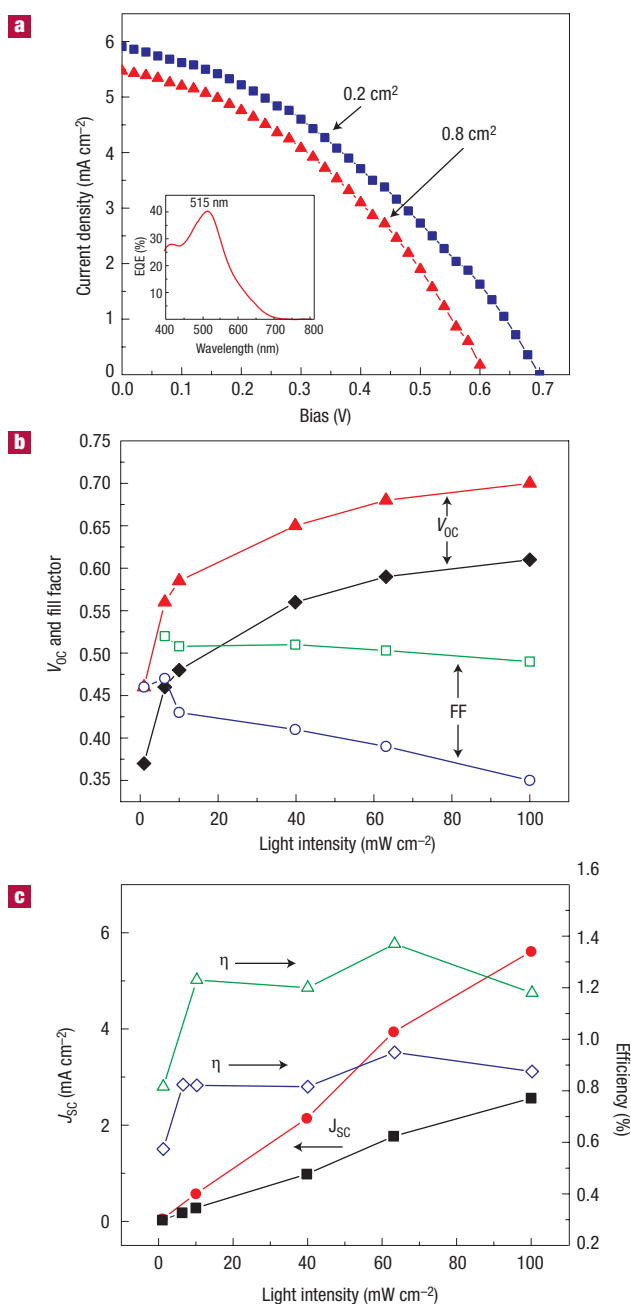
Figure 2 Device performance under AM 1.5G illumination. a, Traces of current density against voltage (J–V) for two cells with roughness factors of ~200. The small cell (active area: 0.2 cm²) shows a higher V_{oc} and J_{sc} than the large cell (0.8 cm²). The fill factor and efficiency are 0.37 and 1.51% and 0.38 and 1.26%, respectively. Inset, the external quantum efficiency against wavelength for the large cell. **b**, Open-circuit voltage and fill factor against light intensity, and **c**, short-circuit current density and efficiency against light intensity for cells with roughness factors from 75 to 200. Each of the four parameters is represented by data from two different devices in order to provide an estimate of the range of their variability. In general, cells of high roughness factor have low V_{oc} and fill factor, but high J_{sc} and efficiency (see Fig. S7). Note that each of the eight plots is taken from a different device. Active cell size: 0.8 cm².
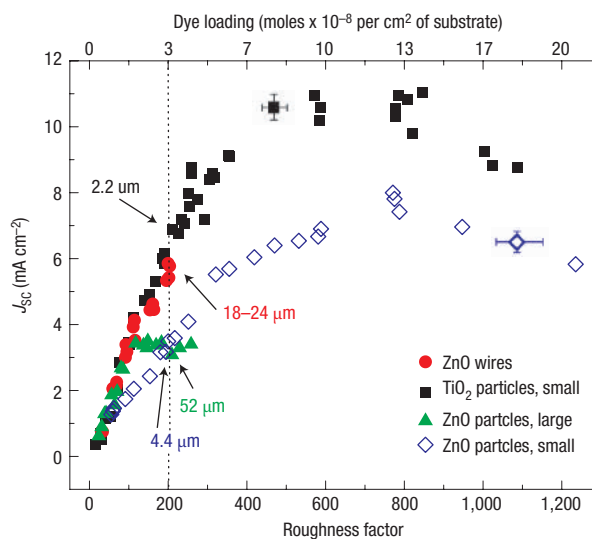

Figure 3 Comparative performance of nanowire and nanoparticle cells. Short-circuit current density versus roughness factor for cells based on ZnO wires, small TiO₂ particles, and large and small ZnO particles. The TiO₂ films show a higher maximum current than either of the ZnO films and a larger initial slope than the small ZnO particles, consistent with better transport through TiO₂ particle networks. The large ZnO particle cells attain a smaller maximum current than the small particles because the film thickness (and therefore the electron escape length) becomes larger than the electron diffusion length at a much lower roughness factor. The wire data fall on the TiO₂ line and significantly exceed the current output from both types of ZnO particle cells above a roughness factor of ~100. A slight sag of the wire data off the TiO₂ line at high roughness factor may be a sign of excessive scattering within the opaque wire films. Cell thickness is directly proportional to roughness factor and is labelled for each cell type at a roughness factor of 200. Error bars are provided on only two points to maximize figure clarity, and they are an estimate of the maximum range of the values. The error bars for cells with roughness factors below 250 are smaller than the size of the data points. Data points were made by measuring the roughness factor of dye-sensitized films through ultraviolet–visible spectroscopy of the desorbed dye in basic H₂O and then re-sensitizing the films for fabrication into cells. See also Fig. S6. Fig. S7 shows comparative trends in η, V_{oc} and fill factor. Cell size: 0.8 cm².

electrolyte (Fig. S3). Thus, facile transport through the nanowire array is retained in device-like environments and should result in faster carrier extraction in the nanowire cell.

Solar cells were constructed with wire arrays of various surface areas and tested in simulated sunlight. At a full Sun intensity of 100 ± 3 mW cm⁻², our highest-surface-area devices are characterized by J_{sc} = 5.3–5.85 mA cm⁻², V_{oc} = 0.61–0.71 V, FF = 0.36–0.38 and efficiency η = 1.2–1.5%. (Fig. 2a) The external quantum efficiency of these cells peaks at 40–43% near the absorption maximum of the dye and is limited chiefly by the relatively low dye loadings of the nanowire films.

Figure 2b and c shows the effect of light intensity on the performance characteristics of the wire cells. The open-circuit voltage and short-circuit current depend logarithmically and linearly on light flux, respectively. The fill factors are low compared with nanoparticle cells, do not vary with cell size (see Fig. S4), and fall off with increasing light intensity owing to the development of a large photo-shunt of unknown origin. These poor fill factors halve the potential efficiency of our best nanowire cells, and they are robust with respect to changes in the nanowire electrical properties (Fig. S5), electrolyte concentration and choice of substrate (FTO or
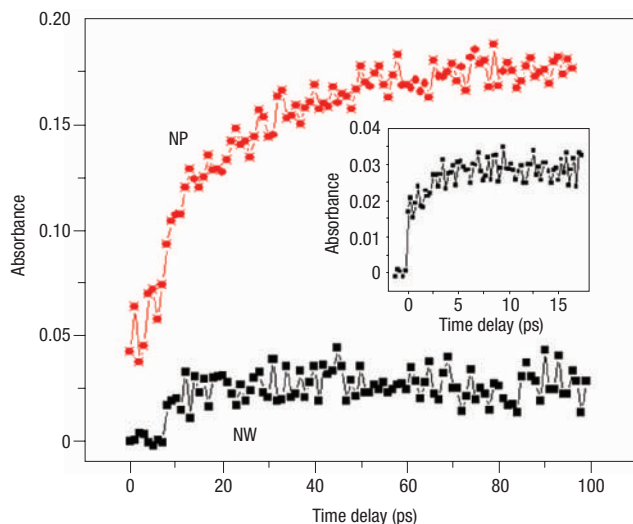
Figure 4 Transient mid-infrared absorption traces of dye-sensitized ZnO nanowire (NW) and ZnO nanoparticle (NP) films pumped at 400 nm. The large difference in injection amplitudes is due to the larger surface area of the particle film. Injection in wires is complete after ~5 ps but continues for ~100 ps in the particle case. A high-resolution trace (inset) shows the ultrafast step (<250 fs) and ~3 ps rise time for a nanowire sample. The slower time constant showed a weak dependence on pump wavelength (see Figs S8 and S9). Particles were synthesized[6] and films were prepared[25] (using dye N719) as described elsewhere. Films were deposited on Al_2O_3 substrates. Spectra are offset by ~0.05 absorbance units for clarity.

indium tin oxide). The efficiency of our devices is fairly flat above a power density of ~5 mW cm^{-2}.

To assess the relative efficiency with which carriers are extracted from the nanowire devices, we compare in Fig. 3 the short-circuit current densities of the wire cells to those of TiO$_2$ and ZnO nanoparticle cells as a function of the internal surface area (roughness factor). A hypothetical photoanode that maintained a near-unity carrier collection efficiency independent of roughness factor would trace out a line in this plot that gradually tapered off at high surface areas to a large J_{sc} value (>25 mA cm^{-2}). In contrast, the rapid saturation and subsequent decline of the current from cells built with 12-nm TiO$_2$ particles, 30-nm ZnO particles or 200-nm ZnO particles confirms that the transport efficiency of particle films falls off above a certain film thickness, as we argued above. Crucially, the nanowire films show a nearly linear increase in J_{sc} that maps almost directly onto the TiO$_2$ data. Because transport in the thin TiO$_2$ particle films is very efficient (with J_{sc} = 7.8–8.7 mA cm^{-2} at a roughness factor of 250), this is strong evidence of an equally high collection efficiency for nanowire films as thick as ~25 μm. In addition, the nanowire cells generate considerably higher currents than either of the ZnO particle cells over the accessible range of roughness factors (55–75% higher at a roughness of 200). This is direct confirmation of the superiority of the nanowire photoanode as a charge collector.

Better electron transport within the nanowire photoanode is a product of both its higher crystallinity and an internal electric field that can assist carrier collection by separating injected electrons from the surrounding electrolyte and sweeping them towards the collecting electrode. The Debye–Hückel screening length of ZnO (roughly one-third of the thickness of the space-charge layer in the semiconductor at the semiconductor–electrolyte junction) is about 4 nm for a carrier concentration of 10^{18} cm^{-3}, making our nanowires

thick enough to support the sort of radial electric field (depletion layer) that is impossible in smaller TiO$_2$ or ZnO nanoparticles with fewer carriers. This upward band bending at the nanowire surface should suppress recombination by corralling injected electrons within the wire cores. At the same time, an axial field along each nanowire encourages carrier motion towards the external circuit. These macroscopic fields should act synergistically to increase electron transport relative to nanoparticle cells, which lack such fields. Ambipolar diffusion is consequently a less dominant mechanism in the nanowire devices.

A switch from particles to wires also affects the kinetics of charge transfer at the dye–semiconductor interface, as particle and wire films have dissimilar surfaces onto which the sensitizing dye adsorbs. Whereas ZnO particles present an ensemble of surfaces having various bonding interactions with the dye, our wire arrays are dominated by a single crystal plane (the {100}) that accounts for over 95% of their total area. We used femtosecond transient absorption spectroscopy to measure the rate of electron injection from photoexcited ruthenium dyes into nanowire and nanoparticle films. Dye-sensitized samples were excited with 400-nm, 510-nm or 570-nm pulses and the free carrier concentration of the oxide was monitored with a mid-infrared probe (see Figs S8 and S9). The transient responses for wires and particles (Fig. 4) were considerably different. Injection in wires was characterized by bi-exponential kinetics with time constants of less than 250 fs and around 3 ps, whereas the particle response was tri-exponential and significantly slower (time constants: <250 fs, 20 ps, 200 ps). Our data on particle injection are in excellent agreement with published results[25], validating our evidence for faster electron injection in nanowires.

The nanowire dye-sensitized solar cell is an exciting variant of the most successful of the excitonic photovoltaic devices. As an ordered topology that increases the rate of electron transport, a nanowire electrode may provide a means to improve the quantum efficiency of DSCs in the red region of the spectrum, where their performance is currently limited. Important differences in transport, internal electric field distribution and light scattering should make comparative studies of wire and particle devices fruitful. Raising the efficiency of the nanowire cell to a competitive level depends on achieving higher dye loadings through an increase in surface area. We are now extending our synthetic strategy to design nanowire electrodes with much larger areas available for dye adsorption. The advantages of the nanowire geometry are even more compelling for other types of excitonic photocells, such as inorganic–polymer hybrid devices[26], in which an oriented, continuous and crystalline inorganic phase of the proper dimensions could greatly improve the collection of both electrons and holes.

METHODS

SYNTHESIS OF NANOWIRE ARRAYS

Arrays of ZnO nanowires were synthesized on FTO substrates (TEC-7, 7 Ω per square), Hartford Glass Co.) that were first cleaned thoroughly by acetone/ethanol sonication and then coated with a thin film of ZnO quantum dots, 3–4 nm in diameter, by dip-coating in a concentrated ethanol solution. Nanowires were grown by immersing seeded substrates in aqueous solutions containing 25 mM zinc nitrate hydrate, 25 mM hexamethylenetetramine and 5–7 mM polyethylenimine (branched, low molecular weight, Aldrich) at 92 °C for 2.5 hours. Because nanowire growth slowed after this period, substrates were repeatedly introduced to fresh solution baths in order to obtain long wire arrays (total reaction times of up to 50 hours). The arrays were then rinsed with deionized water and baked in air at 400 °C for 30 minutes to remove any residual organics and to optimize cell performance.

SOLAR CELL FABRICATION AND CHARACTERIZATION

Nanowire arrays were first sensitized in a solution (0.5 mmol l^{-1}) of (Bu$_4$N)$_2$Ru(dcbpyH)$_2$(NCS)$_2$ (N719 dye) in dry ethanol for one hour and then sandwiched together and bonded with thermally platinized FTO counter electrodes separated by 40-μm-thick hot-melt spacers (Bynel, Dupont). The internal space of the cell was filled with a liquid electrolyte (0.5 M LiI, 50 mM I$_2$, 0.5 M 4-tertbutylpyridine in 3-methoxypropionitrile (Fluka)) by capillary action. Cells were immediately tested under AM 1.5G simulated sunlight (300 W Model 91160, Oriel). Intensity measurements were made with a set of neutral density filters. External quantum efficiency (EQE) values (uncorrected for transmission and reflection losses) were obtained with a 150-W xenon lamp coupled to a monochromator, and calibrated with a silicon photodiode.

Identical procedures were used to build and test DSCs based on TiO_2 and ZnO particle films prepared by spin-coating or spreading pastes with a thin glass rod (doctor-blading). Films of TiO_2 made from a commercial paste of 10–15-nm anatase crystals (Ti-Nanoxide T, Solaronix) were sintered at 450 °C for 30 minutes, treated with a 0.2 M aqueous $TiCl_4$ solution for 12 hours as described previously[2], sintered a second time at 450 °C for 30 minutes and sensitized with dye for 24 hours. Pastes of small, spherical ZnO particles (30 ± 14 nm) and large, irregular ZnO particles (200 ± 75 nm) were formulated as described previously[27], and sintered and sensitized similarly to the nanowire cells. Film thickness was varied by using different spacers for doctor-blading and/or by diluting the pastes with water. All films were free of cracks. The small ZnO particles were synthesized by heating 0.8 g zinc acetate dihydrate and 50 ml ethanol in an autoclave at 125 °C for 2 hours. The large particles were obtained as a commercial powder (200 mesh, 99.999%, Cerac).

ELECTRICAL MEASUREMENTS

For the single wire studies, nanowires 8–10 µm long were dispersed from ethanol solution on oxidized silicon substrates (300 nm SiO_2) and fired in air at 400 °C for 30 minutes. Electron-beam lithography was used to pattern and deposit contacts (100 nm Ti) linking the wires to prefabricated electrode sets. Most devices showed ohmic I–V plots without annealing treatments. Measurements were made with a global back gate using a semiconductor parameter analyser (4145B, Hewlett-Packard). Samples for array transport studies were made by encapsulating fired arrays (grown on FTO) in a matrix of spin-cast poly(methylmethacrylate) (PMMA), exposing the wire tips by ultraviolet development and dissolution of the top portion of the PMMA film, and then depositing metal contacts by thermal evaporation. The insulating PMMA matrix prevented potential short circuits due to pinholes in the nanowire array and provided mechanical stability for the measurement.

MID-INFRARED TRANSIENT ABSORPTION MEASUREMENTS

Transient absorption measurements were made with a home-built Ti:sapphire oscillator (30 fs, 88 MHz) and commercial regenerative amplifier (Spitfire, Spectra-Physics) that operates at 810 nm and 1 kHz repetition rate. About 800 µJ of the beam was used to pump an optical parametric amplifier (TOPAS, Quantronix), while 80 J was retained and frequency-doubled in β-barium borate (BBO) for use as the 405-nm pump beam. This beam was delayed by a motorized stage and directed to the sample. The signal and idler beams from the optical parametric amplifier were combined in a $AgGaS_2$ crystal to create tuneable mid-infrared pulses (1,000–3,500 cm^{-1}). The residual 810-nm beam and the residual signal and idler beams were re-combined in a BBO crystal to create sum-frequency generation at 510 nm and 575 nm. The 510-nm beam was directed to a separate delay stage and then to the sample. The pump beams were focused to a spot size of roughly 200–300 µm, with typical pump energies of 0.5–2 µJ. The pump beams were mechanically chopped at 500 Hz (synchronous with the laser), and separate boxcar integrators were triggered by the rejected and passed beams, allowing for independent detection channels of probe with pump ('sample') and without pump ('reference'). The sample signal was subtracted from the reference signal, and the result was divided by the reference to give the differential transmittance, which was converted to effective absorbance. The probe beam, which was typically centred at 2,150 cm^{-1} with a bandwidth of 250 cm^{-1}, was focused with a CaF_2 lens to a size of roughly 100–200 µm. The probe beam was collected after transmission through the sample and directed through bandpass filters before being focused onto a single-element HgCdTe detector (IR Associates). An instrument response of 250–300 fs was determined by measuring the rise of free-electron absorption (less than 50 fs) in a thin silicon wafer after blue or green pump.

Each transient plot is an average of points taken on both forward and reverse scans, checked for reproducibility. Each point consists of about 500 averaged laser shots. Samples were translated after each scan to minimize probing dye photoproducts. They were not moved during the scan because small inhomogeneities caused changes in the amplitude of the transient signal, obscuring the true kinetics.

References

1. Gregg, B. A. Excitonic solar cells. *J. Phys. Chem. B* **107,** 4688–4698 (2003).
2. Nazeeruddin, M. K. *et al.* Engineering of efficient panchromatic sensitizers for nanocrystalline TiO_2-based solar cells. *J. Am. Chem. Soc.* **123,** 1613–1624 (2001).
3. Wang, P. *et al.* A stable quasi-solid-state dye-sensitized solar cell with an amphiphilic ruthenium sensitzer and polymer gel electrolyte. *Nature Mater.* **2,** 402–407 (2003).
4. Rensmo, H. *et al.* High light-to-energy conversion efficiencies for solar cells based on nanostructured ZnO electrodes. *J. Phys. Chem. B* **101,** 2598–2601 (1997).
5. Tennakone, K., Kumara, G. R. R. A., Kottegoda, I. R. M. & Perera, V. P. S. An efficient dye-sensitized photoelectrochemical solar cell made from oxides of tin and zinc. *Chem. Commun.* 15–16 (1999).
6. Keis, K., Magnusson, E., Lindström, H., Lindquist, S.-E. & Hagfeldt, A. A 5% efficient photoelectrochemical solar cell based on nanostructured ZnO electrodes. *Sol. Energy Mater. Sol. Cells* **73,** 51–58 (2002).
7. Krüger, J., Plass, R., Grätzel, M., Cameron, P. J. & Peter, L. M. Charge transport and back reaction in solid-state dye-sensitized solar cells: a study using intensity-modulated photovoltage and photocurrent spectroscopy. *J. Phys. Chem. B* **107,** 7536–7539 (2003).
8. O'Regan, B. & Grätzel, M. A low-cost, high-efficiency solar cell based on dye-sensitized colloidal TiO_2 films. *Nature* **353,** 737–740 (1991).
9. Fisher, A. C., Peter, L. M., Ponomarev, E. A., Walker, A. B. & Wijayantha, K. G. U. Intensity dependence of the back reaction and transport of electrons in dye-sensitized nanocrystalline TiO_2 solar cells. *J. Phys. Chem. B* **104,** 949–958 (2000).
10. Oekermann, T., Zhang, D., Yoshida, T. & Minoura, H. Electron transport and back reaction in nanocrystalline TiO_2 films prepared by hydrothermal crystallization. *J. Phys. Chem. B* **108,** 2227–2235 (2004).
11. Nelson, J. Continuous-time random-walk model of electron transport in nanocrystalline TiO_2 electrodes. *Phys. Rev. B* **59,** 15374–15380 (1999).
12. van de Lagemaat, J. & Frank, A. J. Nonthermalized electron transport in dye-sensitized nanocrystalline TiO_2 films: transient photocurrent and random-walk modeling studies. *J. Phys. Chem. B* **105,** 11194–11205 (2001).
13. Kopidakis, N., Schiff, E. A., Park, N.-G., van de Lagemaat, J. & Frank, A. J. Ambipolar diffusion of photocarriers in electrolyte-filled, nanoporous TiO_2. *J. Phys. Chem. B* **104,** 3930–3936 (2000).
14. Benkstein, K. D., Kopidakis, N., van de Lagemaat, J. & Frank, A. J. Influence of the percolation network geometry on electron transport in dye-sensitized titanium dioxide solar cells. *J. Phys. Chem. B.* **107,** 7759–7767 (2003).
15. Kopidakis, N., Benkstein, K. D., van de Lagemaat, J. & Frank, A. J. Transport-limited recombination of photocarriers in dye-sensitized nanocrystalline TiO_2 solar cells. *J. Phys. Chem. B* **107,** 11307–11315 (2003).
16. Kavan, L., Grätzel, M., Gilbert, S. E., Klemenz, C. & Schell, H. J. Electrochemical and photoelectrochemical investigation of single-crystal anatase. *J. Am. Chem. Soc.* **118,** 6716–6723 (1996).
17. Wagner, P. & Helbig, R. Hall effect and anisotropy of the mobility of the electrons in zinc oxide. *J. Phys. Chem. Sol.* **35,** 327–335 (1974).
18. Nakade, S. *et al.* Dependence of TiO_2 nanoparticle preparation methods and annealing temperatures on the efficiency of dye-sensitized solar cells. *J. Phys. Chem. B* **106,** 10004–10010 (2002).
19. Frank, A. J., Kopidakis, N. & van de Lagemaat, J. Electrons in nanostructured TiO_2 solar cells: transport, recombination and photovoltaic properties. *Coord. Chem. Rev.* **248,** 1165–1179 (2004).
20. Renouard, T. *et al.* Novel ruthenium sensitizers containing functionalized hybrid tetradentate ligands: synthesis, characterization, and INDO/S analysis. *Inorg. Chem.* **41,** 367–378 (2002).
21. Hara, K. *et al.* Design of new coumarin dyes having thiophene moieties for highly efficient organic-dye-sensitized solar cells. *New J. Chem.* **27,** 783–785 (2003).
22. Kron, G., Egerter, T., Werner, J. H. & Rau, U. Electronic transport in dye-sensitized nanoporous TiO_2 solar cells—comparison of electrolyte and solid-state devices. *J. Phys. Chem. B* **107,** 3556–3564 (2003).
23. Greene, L. *et al.* Low-temperature wafer scale production of ZnO nanowire arrays. *Angew. Chem. Int. Edn Engl.* **42,** 3031–3034 (2003).
24. Noack, V., Weller, H. & Eychmüller, A. Electron transport in particulate ZnO electrodes: a simple approach. *J. Phys. Chem. B.* **106,** 8514–8523 (2002).
25. Anderson, N. A., Ai, X. & Lian, T. Electron injection dynamics from Ru polypyridyl complexes to ZnO nanocrystalline thin films. *J. Phys. Chem. B* **107,** 14414–14421 (2003).
26. Huynh, W. U., Dittmer, J. J. & Alivisatos, A. P. Hybrid nanorod–polymer solar cells. *Science* **295,** 2425–2427 (2002).
27. Park, N.-G. *et al.* Morphological and photoelectrochemical characterization of core–shell nanoparticle films for dye-sensitized solar cells: Zn-O type shell on SnO_2 and TiO_2 cores. *Langmuir* **20,** 4246–4253 (2004).

Competing financial interests

The authors declare that they have no competing financial interests.